

Structure-driven intercalated architecture of septuple-atomic-layer MA_2Z_4 family with diverse properties from semiconductor to topological insulator to Ising superconductor

Lei Wang,^{1,2} Yongpeng Shi,^{1,2} Mingfeng Liu,^{1,2} Yi-Lun Hong,^{1,2} Ming-Xing Chen,³ Ronghan Li,^{1,2} Qiang Gao,^{1,2} Wencai Ren,^{1,2} Hui-Ming Cheng,^{1,2,4} Yiyi Li,^{1,2} and Xing-Qiu Chen^{1,2,*}

¹Shenyang National Laboratory for Materials Science, Institute of Metal Research, Chinese Academy of Science, 110016 Shenyang, Liaoning, P. R. China

²School of Materials Science and Engineering, University of Science and Technology of China, Shenyang 110016, P. R. China

³School of Physics and Electronics, Hunan Normal University, Changsha 410081, P. R. China

⁴Shenzhen Geim Graphene Center, Tsinghua-Berkeley Shenzhen Institute (TBSI), Tsinghua University, 1001 Xueyuan Road, Shenzhen 518055, P. R. China

(Dated: August 10, 2020)

Motivated by the fact that septuple-atomic-layer $MnBi_2Te_4$ can be structurally viewed as the combination of double-atomic-layer $MnTe$ intercalating into quintuple-atomic-layer Bi_2Te_3 , we present a general approach of constructing twelve septuple-atomic-layer α_i - and β_i - MA_2Z_4 monolayer family ($i = 1$ to 6) by intercalating MoS_2 -type MZ_2 monolayer into $InSe$ -type A_2Z_2 monolayer. Besides reproducing the experimentally synthesized α_1 - $MoSi_2N_4$, α_1 - WSi_2N_4 and β_5 - $MnBi_2Te_4$ monolayer materials, another 66 thermodynamically and dynamically stable MA_2Z_4 were predicted, which span a wide range of properties upon the number of valence electrons (VEC). MA_2Z_4 with the rules of 32 or 34 VEC are mostly semiconductors with direct or indirect band gap and, however, with 33 VEC are generally metal, half-metal ferromagnetism, or spin-gapless semiconductor upon whether or not an unpaired electron is spin polarized. Moreover, we propose α_2 - WSi_2P_4 for the spin-valley polarization, α_1 - $TaSi_2N_4$ for Ising superconductor and β_2 - $SrGa_2Se_4$ for topological insulator.

Due to the potential applications in energy storage and conversion^{1,2}, nanoelectronics^{3,4}, and spintronics^{5,6}, as well as superconductivity⁷⁻¹⁶, two-dimensional (2D) hexagonal monolayer materials have been attracting tremendous interest in both experimental and theoretical studies, which is inseparable from their rich geometric structures and chemical compositions.

To dates, some 2D monolayer materials have been discovered while their atomic-layer numbers are limited to just a few. In 2004, the single atomic layer ($n = 1$) graphite in Fig. 1(a), namely graphene, was experimentally realized by mechanical exfoliation method, giving rise to the birth of 2D materials. Graphene is a semimetal with the occurrence of massless Dirac cone due to the σ bonding hopping, leading to a few special properties, *e.g.* ultra-high carrier mobility¹⁷, high mechanical strength¹⁸, high thermal conductivity¹⁹ and high optical transparency^{20,21}. In similarity to graphene from graphite, one-atomic-layer h -BN monolayer can also be exfoliated from its bulk form, but with a wide gap of about 6 eV^{22,23}. When two carbon atoms of graphene in its unit cell are replaced by Si, Ge or Sn atom, its flat $n = 1$ monolayer structure will be slightly buckled into a double-atomic-layer $n = 2$ monolayer structure in Fig. 1(a). When n comes to three, monolayer transition metal dichalcogenides (TMDCs)^{24,25} become highly rich in both compositions and properties, spanning a wide range from semimetals, semiconductors, and to superconductors as well as to topological insulators. For example, $n = 3$ $2H$ - WTe_2 monolayer (Fig. 1(a)) is predicted to be a weyl semimetal^{26,27} with an anomalous giant magnetoresistance and superconductivity²⁸, while that its distorted $1T$ monolayer structure is predicted to be a quantum spin Hall (QSH) insulator²⁹. Another type of $n = 3$ monolayer material is the recently discovered van der Waals (vdW) 2D ferromagnetic semiconductor CrI_3 , with a very large tunneling

magnetoresistance, of which the magnetism can be manipulated by the bias electric field and electrostatic doping³⁰⁻³². Monolayer $InSe$ (Fig. 1(a)) of group-III monochalcogenides³³ consisting of quadruple-atomic-layer $n = 4$ monolayer can be used in photocatalyst³⁴ and the hole-doped monolayer $InSe$ even has a strong electron-phonon coupling, which affects its transport and optical properties^{35,36}. As to the quintuple-atomic-layer $n = 5$ monolayer structure (Fig. 1(a)), Bi_2Se_3 is a famous case of topological insulator (TI)^{37,38}. Another $n = 5$ monolayer $CrGeTe_3$ is also a vdW 2D magnet with the potential to be applied in ultra-compact spintronics³⁹. Furthermore, the known sextuple-atomic-layer $n = 6$ monolayer material (*e.g.*, $CaMg$ in Fig. 1(a)) was theoretically predicted in the reported 2D MatPedia database⁴⁰. With further increasing atomic layer n , the vdW $MnBi_2Te_4$ and septuple-atomic-layer $n=7$ $MnBi_2Te_4$ monolayer (Fig. 1(a)) were reported to be the antiferromagnetic and ferromagnetic topological insulators, respectively⁴¹⁻⁴⁴, which naturally possesses anomalously quantum spin Hall effect⁴⁵. Most recently, another type of $n = 7$ monolayer material of $MoSi_2N_4$ (Fig. 1(a)) has been reported, which is a semiconductor with a band gap of about 1.94 eV⁴⁶. As illustrated in Fig. 1(a), these known monolayer 2D materials consisting of $n = 1, 2, 3, 4, 5, 6$, and 7 atomic layer thicknesses have attracted tremendous interest for their structures, physics and potential applications. Certainly, there is no doubt that, with varying n number, compositions and constituents, they will become richer in both structures and properties. However, the difficulties lie in how we effectively seek for more monolayer materials with promising properties.

Within this context, we have proposed a general intercalated architecture approach to systemically construct $n=7$ MA_2Z_4 monolayer family on basis of first-principles density functional theory. Besides reproducing the experimentally synthesized α_1 - $MoSi_2N_4$, α_1 - WSi_2N_4 and β_5 - $MnBi_2Te_4$

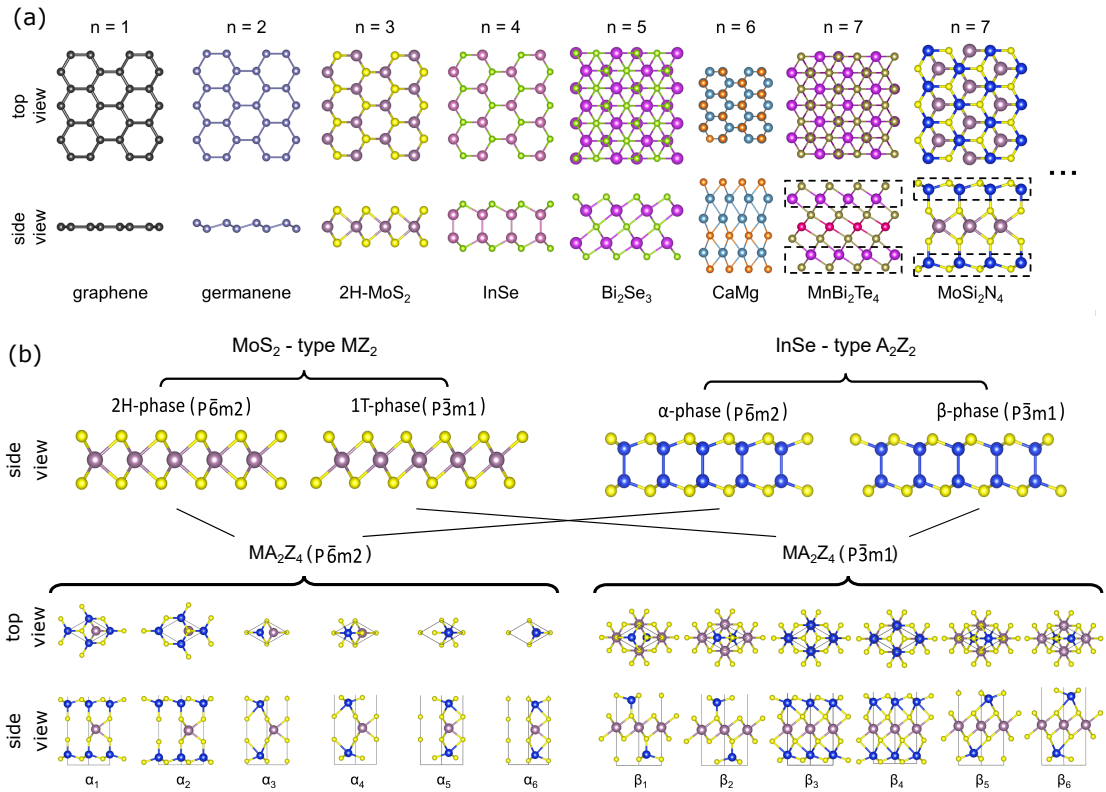


FIG. 1. (Color online) Panel (a), Representatives for 2D materials with increasing atomic-layer number, “ n ”. Panel (b), twelve possible constructions (α_i and β_i $n=7$ monolayer structure, $i=1, 6$) by intercalating MoS₂-type MZ_2 $n=3$ monolayer into broken InSe-type A_2Z_2 $n=4$ monolayer. Note that all α_i and β_i $n=7$ monolayer structures share the same space groups of $P\bar{6}m2$ and $P\bar{3}m1$, respectively.

monolayer materials, we predict 66, thermodynamically and dynamically, stable MA_2Z_4 monolayer materials with diverse properties, which can be classified via the number of valence electrons (VEC). MA_2Z_4 with the rules of 32 or 34 VEC are mostly semiconductors with direct or indirect band gap and, however, with 33 VEC are generally metal, half-metal ferromagnetism, or spin-gapless semiconductor upon whether or not an unpaired electron is spin polarized. Additionally, we suggest α_2 -WSi₂P₄ monolayer material for the spin-valley polarization, α_1 -TaSi₂N₄ for Ising superconductor and β_2 -SrGa₂Se₄ for topological insulator.

I. RESULTS

Intercalated architecture approach. If we look back these known 2D monolayer materials in Fig. 1(a), they seem to share a general scheme (here called *intercalated architecture*) to construct various 2D structures within atomistic scale. A $n=7$ MnBi₂Te₄ monolayer was viewed as the (111) plane of rocksalt structure MnTe inserted into the $n=5$ Bi₂Se₃ monolayer^{37,38}. In a sense, it seems inherit the topology of Bi₂Se₃ and the magnetism of MnTe. By analyzing $n=7$ MoSi₂N₄ monolayer, it can be viewed as the insertion of the $n=3$ 2H-MoS₂-type MoN₂ monolayer into the $n=4$ α -InSe-type Si₂N₂

monolayer⁴⁷. With such a special insertion and structural stacking, monolayer MoSi₂N₄ seems to inherit the semiconducting gap of α -Si₂N₂ (1.74 eV derived by PBE⁴⁷) and interesting tunable properties from MoS₂-type MoN₂. Importantly, MoS₂-type monolayer has two frequently observed $n=3$ 2H ($P\bar{6}m2$) and 1T ($P\bar{3}m1$) monolayer structures, and InSe-type monolayer usually crystallizes in two prototypical $n=4$ α ($P\bar{6}m2$) and β ($P\bar{3}m1$) monolayer structures⁴⁷. Hence, we elucidate this process of intercalated architecture in Fig. 1(b) in a more general way. Within the assumption of the same space group for two intercalating monolayer units: (1) 2H-MoS₂-type MZ_2 monolayer can be inserted into α -InSe-type A_2Z_2 monolayer within the same $P\bar{6}m2$ space group to form six possible $n=7$ α_i - MA_2Z_4 monolayer structures ($i=1$ to 6 in the left six panels of Fig. 1(b)); (2) 1T-MoS₂-type MZ_2 monolayer can be inserted into β - A_2Z_2 monolayer within the same ($P\bar{3}m1$) space group to also form the other six possible $n=7$ β_i - MA_2Z_4 monolayer structures ($i=1$ to 6 in the right six panels of Fig. 1(b)). It needs to be emphasized that these six α_i and six β_i ($i=1-6$) monolayer structures indeed connect to each other through mirror and translation operations of double layer unit AZ , respectively.

As a benchmark of the structural modeling reliability, we have first tested the first-principle structural optimizations (supplementary materials⁴⁸) of three experimentally already-

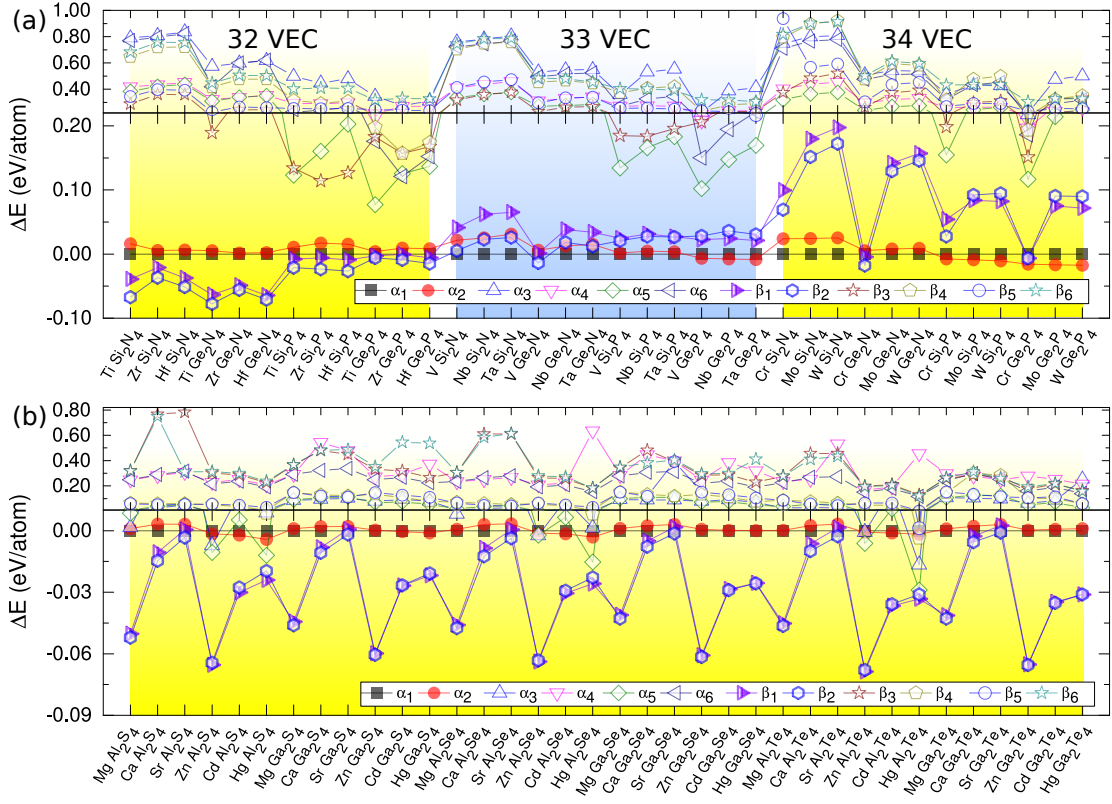


FIG. 2. The DFT-derived enthalpies of formation of 12 competing structural candidates with respect to that of α_1 candidate for 36 MA_2Z_4 monolayer materials with M = first transition metal elements with 32, 33, and 34 VECs in panel (a) and alkali earth elements with 32 VEC in panel (b), respectively.

synthesized $n=7$ monolayer materials of $MnBi_2Te_4$ ^{41–44}, $MoSi_2N_4$ and WSi_2N_4 ⁴⁶ by considering these 12 possible structural candidates. Our calculations reveal that the α_1 -monolayer structure is energetically favorable for both $MoSi_2N_4$ and WSi_2N_4 , whereas the β_5 monolayer structure is the most stable one for $MnBi_2Te_4$ monolayer. The obtained structures for them are in perfect agreement with the known experiments^{41–44}.

Prediction of MA_2Z_4 family. Furthermore, we have extended our DFT structural optimizations by considering a large number of $n=7$ MA_2Z_4 monolayer family by varying atomic constituents (M – the transition metal elements IVB, VB and VIB groups; A – IVA-group elements and Z – VA-group elements). Utilizing DFT calculations, we have performed the structural optimizations by considering all 12 monolayer candidates constructed above for each composition. As shown in Fig. 2(a), we have compiled the relative enthalpies of formations of MA_2Z_4 ($M = Ti, Zr, Hf, V, Nb, Ta, Cr, Mo, W$; $A = Si$ and Ge ; $Z = N$ and P) with respect to their α_1 candidate. Interestingly, we have found that their stabilities in energy seem to be correlated with the number of the valence electrons per formula unit (VEC). MA_2Z_4 monolayer with 32 VEC are all stable at its β_2 phase in Fig. 2(a), but in the series of 33 or 34 VEC the structural stabilities become a bit complicated. MSi_2N_4 ($M = V, Nb, Ta, Cr, Mo, W$,

MGe_2N_4 ($M = Nb, Ta, Mo, W$), and MSi_2P_4 ($M = V, Nb, Ta$) are energetically the lowest in their α_1 monolayer structure, whereas MSi_2P_4 ($M = Cr, Mo, W$) and MGe_2P_4 ($M = V, Nb, Ta, Cr, Mo, W$) are energetically most favorable in their α_2 monolayer phase. The obtained absolute enthalpies of formation and their corresponding optimized lattice constants and structural parameters are further compiled in supplementary Table S1 and S2⁴⁸, respectively. Moreover, we have calculated their phonon dispersions of all these 36 compounds in supplementary Fig. S1⁴⁸. Among them, 32 compounds are stable, both dynamically and thermodynamically, and only 4 compounds (β_2 - $TiSi_2N_4$, β_2 - $TiGe_2N_4$, β_2 - VGe_2N_4 and β_2 - $CrGe_2N_4$) are dynamically unstable, due to their imaginary phonon dispersions.

In addition, we have paid our attention to the other 36 MA_2Z_4 monolayer materials with 32 VEC ($M =$ alkali earth elements (Mg, Ca, Sr) and the IIB-group elements (Zn, Cd, Hg), $A = Al$ and Ga , and $Z = S, Se$, and Te). As shown in Fig. 2(b), all these monolayer materials crystallize in the most stable β_1 or β_2 structures. Fortunately, we have found that among these 36 predictions only β_1 - $ZnAl_2S_4$ was already mentioned in the reported 2DMatPedia database which were obtained through conventional high-throughput computational method via both top-down and bottom-up discovery procedures⁴⁰. This fact further demonstrates the power and

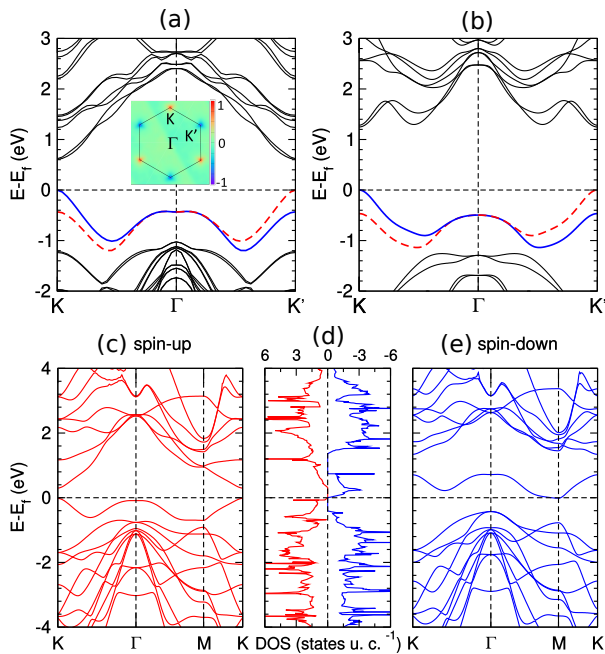


FIG. 3. (color online) (a) Spin-valley coupling of α_2 - WSi_2P_4 in comparison with $2H$ - WSe_2 in (b). Inset of panel (a): Derived Berry curvatures of α_2 - WSi_2P_4 . (c and e) the calculated electronic band structures for the majority spin-up and minority spin-down channels of the spin-gapless α_1 - VSi_2P_4 monolayer semiconductor, along together with their corresponding electronic densities of states in panel (d).

reliability of our currently proposed intercalated architecture.

Electronic structures. We have derived their electronic band structures for these selected 36 compounds in Fig. 2(a) at their most stable structures in supplementary Fig. S2⁴⁸. MA_2Z_4 monolayer with 32 VEC are predicted to be semiconductor for all nitrogen-based compounds, whereas is metallic for all phosphorus-based compounds. We have also noted that, except for a magnetic CrGe_2N_4 , $MA_2\text{N}_4$ with 34 VEC is also semiconductor. It can be understandable for the occurrence of semiconductors, according to the ionic picture satisfying the closed-shell electronic configuration of M^{4+} , A^{4+} , and Z^{3-} for 32 VEC for $M = \text{IVB}$ -group Ti, Zr, and Hf elements or 34 VEC for $M = \text{VIB}$ -group Cr, Mo and W elements due to a remained fully occupied s^2 orbital. Although phosphorus-based compounds with 32 VEC also form closed-shell electron configuration, they are metallic mainly because phosphorus atom has a lower electronegativity than that of nitrogen. We have summarized their band gaps of 17 semiconducting monolayer materials in supplementary Table S2⁴⁸. Four materials of β_2 - ZrGe_2N_4 and β_2 - HfGe_2N_4 and α_2 - MoSi_2P_4 and α_2 - WSi_2P_4 are a direct band-gap semiconductor. The other 13 compounds exhibit the indirect band gaps mostly from the highest valence top at Γ to the lowest conduction bottom at M and K within the framework of the conventional DFT calculations. Their direct band gaps are estimated to be 1.04 eV at Γ , 1.15 eV at Γ , 0.91 eV at K and 0.86 eV at K

for β_2 - ZrGe_2N_4 , β_2 - HfGe_2N_4 , α_2 - MoSi_2P_4 and α_2 - WSi_2P_4 , respectively. Due to conventional DFT problem to underestimate band gap, we have further used hybrid DFT (HSE06) method to correct their band gaps to 2.34 eV, 2.45 eV, 1.19 eV and 1.11 eV, respectively. The case of α_1 - WSi_2N_4 has the largest indirect band gap of 2.08 eV (HSE: 2.66 eV). Although within the framework of conventional DFT three compounds of α_1 - CrSi_2N_4 , α_2 - CrSi_2P_4 and α_2 - WGe_2P_4 are indirect band-gap semiconductors, the HSE calculations revise them to the appearance of direct band gaps of 0.94 eV at K , 0.65 eV at K and 0.89 eV at K , respectively (supplementary Table S2⁴⁸).

VEC of 32 and 34. Similar to the monolayer of TMDCs⁴⁹, our materials of MA_2Z_4 with 32 or 34 VEC are also lacking of inversion symmetry with a strong spin orbit coupling (SOC) effect from the heavy elements M . Hence, many of them are expected to exhibit rich spin-valley physics. Taking α_2 - WSi_2P_4 as an example (Fig. 3(a)), the two valleys at K (K') are the valence band maximum (VBM) and the conduction band minimum (CBM), respectively. The VBM has twofold advantages: In the first there exists a large SOC-induced valley-contrasting spin splitting of about 0.41 eV, which is comparable to that of $2H$ - WSe_2 monolayer^{50,51} in Fig. 3(b). In the second, the VBM at K (K') is 0.4 eV higher than that at Γ and it is robust against strain or layer hybridization, which provides a large space for hole doping to investigate spin-valley physics. Our calculations reveal a Berry curvature contrasting behavior at K and K' (Inset of Fig. 3(a)), which definitely gives rise to the strong valley Hall effect flowing to opposite transverse edges when an in-plane electric field is applied⁵² and also leads to a stronger valley-dependent optical selection rule at both K and K' points⁵³. Furthermore, it exhibits a large hole mobility up to about $460 \text{ cm}^2 \text{ V}^{-1} \text{ s}^{-1}$ and the electron mobility to about $150 \text{ cm}^2 \text{ V}^{-1} \text{ s}^{-1}$ for both the armchair and zigzag directions (supplementary Fig. S3 and Table S4⁴⁸). These values are about one and a half times those of $2H$ - WSe_2 monolayer^{54,55}.

Similarly, among MA_2Z_4 monolayer with 32 VEC ($M =$ alkali earth elements (Mg, Ca, Sr) and the IIB-group elements (Zn, Cd, Hg), $A =$ Al and Ga, and $Z =$ S, Se, and Te), they are mostly semiconductor in supplementary Fig. S7 and Table S3⁴⁸ also due to the closed-shell electronic configurations of M^{2+} , A^{3+} and Z^{2-} . Of course, with increasing atomic mass their band gaps close to become metallic (see supplementary Fig. S7⁴⁸). During this process, extensive topological phase transition occurs. For instance, in Fig. 4 (a, b, d, and e), we have compiled the DFT-derived electronic band structures of two selected monolayer materials of β_2 - SrGa_2S_4 and β_2 - SrGa_2Se_4 without and with the inclusion of the SOC effect. It can be clearly seen that the case of β_2 - SrGa_2S_4 is a direct band gap semiconductor with a gap of about 0.6 eV and 0.5 eV at Γ without and with the SOC inclusion, respectively. However, in the case of its isoelectronic β_2 - SrGa_2Se_4 without the SOC inclusion it is a zero-gap semiconductor due to the degenerate Se- p_x and p_y orbits exactly crossing the Fermi level. With the SOC inclusion, its zero gap become open again with a small gap value of about 68 meV. Importantly, in the case β_2 - SrGa_2S_4 its CBM at Γ comprises with Ga s -like orbit

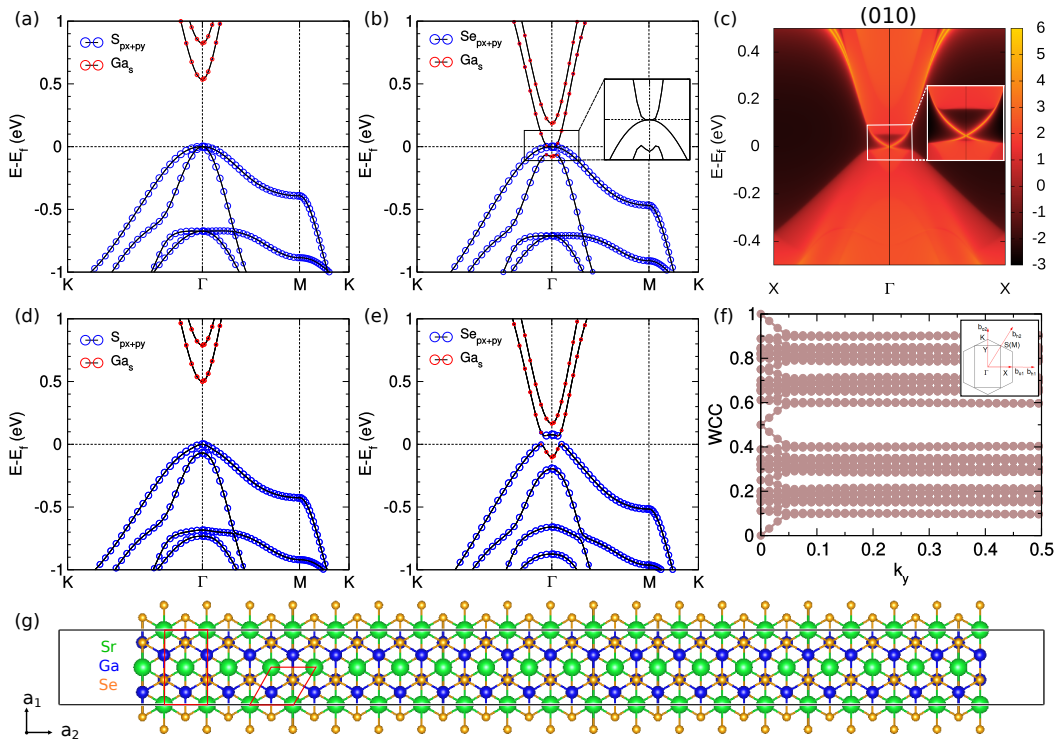


FIG. 4. (Color online) Panel (a),(b) and (d), (e) are electronic band structures without and with including SOC of β_2 -SrGa₂S₄ and β_2 -SrGa₂Se₄, respectively. The insert in Panel (b) shows band degeneracy at Fermi level. Panel (c) is edge states of (010) edge of orthogonal cell and the insert shows the linear dispersive edge states. Panel (f) is evolution of Wannier charge center (WCC) in the $k_z = 0$ plane, which implies a nonzero topological invariant. The insert in Panel (f) is the BZ of hexagonal cell and orthogonal cell. Panel (g) is the top view of 20-cell β_2 -SrGa₂Se₄ nanoribbon with (010) edge, where the red solid-line square and rhombus are orthogonal cell and hexagonal cell, respectively.

and the VBM consists of degenerate $p_{x,y}$ orbitals of S. In contrast, in β_2 -SrGa₂Se₄ we have observed an opposite situation at Γ the CBM has the degenerate $p_{x,y}$ orbitals of Se, whereas the VBM now becomes the Ga s -like orbital. This fact demonstrates the occurrence of the electronic band inversion, implying the possible topological non-trivial feature. Hence, we have calculated their topological index of Z_2 value, indicating $Z_2 = 0$ for trivial β_2 -SrGa₂S₄ semiconductor and $Z_2 = 1$ for non-trivial β_2 -SrGa₂Se₄. This analysis is confirmed by the evolution of Wannier charge center shown in Fig 4(f), thereby indicating that β_2 -SrGa₂Se₄ monolayer material is a topological insulator. Furthermore, this monolayer topological insulator of β_2 -SrGa₂Se₄ has to exhibit non-trivial topological edge states. As shown in Fig. 4(c), we have derived the edge states along the $\langle 010 \rangle$ boundary using the slab modeling in Fig. 4(g), which indicates clear topological helical edge states with the appearance of the Dirac cone. Of course, among all these materials in supplementary Fig. S7 and Fig. S8⁴⁸, some of them can be attributed to be topological insulators, such as β_2 -CaGa₂Se₄ and β_2 -MgGa₂Te₄ and some are topological semimetals, such as HgGa₂Se₄, HgAl₂Te₄ and MGa₂Te₄ ($M = \text{Mg, Ca, Sr, Zn, Cd, and Hg}$).

VEC of 33. In difference from the systems with 32 or 34 VEC, MA_2Z_4 monolayer materials with 33 VEC is very special. This is mainly because of the existence of one more un-

paired electron than 32 VEC and one less than 34 VEC. In the first, the unpaired electron has to cross the Fermi level, leading to the metallic occurrence and, in the second, the one more unpaired electron provides the crucial prerequisites for the onset of magnetic ordering. Our spin-polarized calculations reveal that, in the system of 33 VEC, there are eight ferromagnetic monolayer materials (supplementary Fig. S5⁴⁸). β_2 -VGe₂N₄ is a typical half-metallic ferromagnet with an integer spin moment ($1.0 \mu_B$) that V atom carries, because its spin-up band carries electronic density of states at the Fermi level and its spin-down band is a semiconductor with a band gap. Both α_1 -VSi₂N₄ and α_1 -NbGe₂N₄ seem exactly on the edge of the half-metallic ferromagnetism and both V and Nb atoms carry the nearly integer spin moments of $0.97 \mu_B$ and $0.98 \mu_B$, respectively. In particular, we need to emphasize that α_1 -VSi₂P₄ is a parabolic spin-gapless ferromagnetic semiconductor with a total integer spin moment of $1.0 \mu_B$ ^{56,57} in Fig. 3(c,d,e). Although both majority and minority channels are semiconductor, the VBM of the majority electrons touches the Fermi level at the K or K' points and the CBM of the minority electrons touches the Fermi level as well, but at the M point. This fact means that for an excitation energy up to the band gap energy of the other spin channel, the excited electrons and holes are both 100% spin polarized^{56,57}. Interestingly, if we continuously check MA_2Z_4 monolayer materials

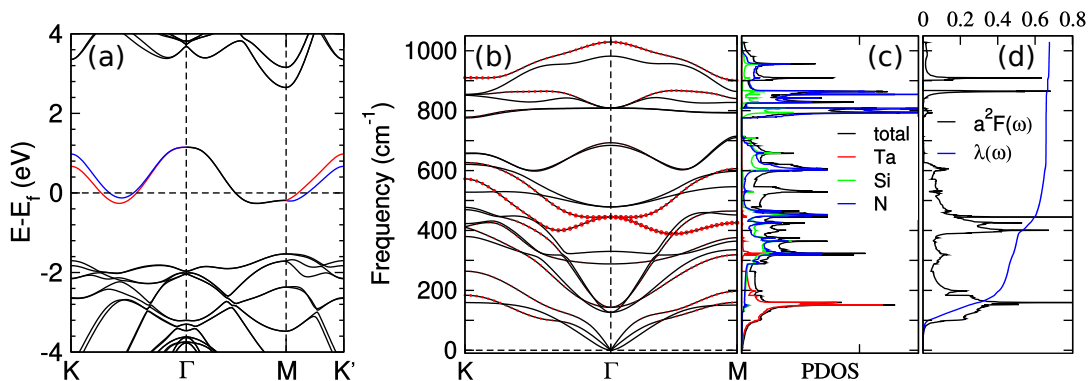


FIG. 5. (Color online) (a) Contrasting spin-up (red) and spin-down (blue) split at both K and K' of α_1 -TaSi₂N₄ due to the SOC-induced Zeeman-like field, which is opposite for the two valleys. (b) The derived phonon dispersion in which the area of the red circles represents the strength of phonon linewidth $\gamma_{q,\nu}$. (c) Phonon DOS and (d) Eliashberg function $\alpha^2 F(\omega)$ with accumulated electron-phonon coupling strength $\lambda(\omega)$.

with its VEC from 32 to 38 in this series of $M = \text{Ti, V, Cr, Mn, Fe, Co, and Ni}$, we have found more half-metallic ferromagnetism satisfying the Slater-Pauling behavior that allows us to estimate the total spin moment via $M_t = 3 - |\text{VEC} - 35| \mu_B$.

Nonmagnetic metallic MA_2Z_4 with 33 VEC are intriguing. Within this kind of nonmagnetic situation of the non-centrosymmetric 2D lattice, an unpaired electron will result in a half-filled electronic band which crosses the Fermi level. Similar to α_2 -WSi₂P₄ monolayer semiconductor in Fig. 3(a), the SOC effect of Ta atom also induces a very large valley-contrasting spin splitting at the K and K' , contributing Zeeman-like spin splittings (Fig. 5(a)). This will be beneficial to the occurrence of Ising superconductivity, as what one already observed in TMDC NbSe₂⁷⁻¹⁴. Following this inspiration, we have further derived the phonon dispersion and Eliashberg function ($\alpha^2 F(\omega)$) as well as accumulated electron-phonon coupling strength (λ) in Fig. 5(b to c) for the nonmagnetic metallic α_1 -TaSi₂N₄. Using the total $\lambda=0.68$ and the calculated logarithmic average phonon frequency of 298.8 cm^{-1} , we have derived the superconductive transition temperature $T_c = 9.67$ K via the Dynes modified McMillan formula with the effective screened Coulomb repulsion constant of $\mu = 0.10$. The superconductive α_1 -TaSi₂N₄ monolayer material is remarkable, because in its noncentrosymmetric lattice with a large SOC splitting spins of Cooper pairs are aligned along the out-of-plane direction in accompanying with a large in-plane upper critical field exceeding the Pauli paramagnetic limit. Its superconductivity effectively does not respond to the in-plane magnetic field, which make its superconductivity robust against a magnetic field⁷⁻¹⁴. Of course, our calculations still reveal that the other two α_2 -TaGe₂P₄ and β_2 -HfGe₂P₄ are superconductor with the estimated T_c of 3.75 K and 1.07 K, as show in supplementary Fig. S6⁴⁸, respectively.

II. CONCLUSION

In this work, we present a general intercalated architecture approach to construct septuple-atomic-layer MA_2Z_4 monolayer materials. Our approach predicts 66 MA_2Z_4 monolayer materials which are stable both thermodynamically and dynamically, among 72 candidates considered here. Interestingly, their electronic properties spans a wide range upon the valence electron number per formula (VEC). MA_2Z_4 monolayer materials with the rules of 32 or 34 VEC are mostly semiconductors with direct or indirect band gap. Upon the spin-orbit coupling strength associated with the atomic mass, topological transitions have been predicted to occur from trivial semiconductors to non-trivial topological insulators, *e.g.*, from trivial semiconductor of β_2 -SrGa₂S₄ to non-trivial topological insulator of β_2 -SrGa₂Se₄ to topological semimetal of β_2 -SrGa₂Te₄. In addition, these 2D semiconductors with non-centrosymmetric in-planar lattices provide plenty of room to study spin-valley coupling physics due to the momentum-contrasting spin-valley splitting and Berry curvatures at K or K' point of the 2D hexagonal BZ corners (*e.g.*, α_1 -WSi₂P₄). We also predict that MA_2Z_4 monolayer materials with 33 VEC are general metal, or half-metal ferromagnetism (*e.g.*, α_1 -VSi₂N₄), or spin-gapless semiconductor (*e.g.*, α_1 -VSi₂P₄) upon whether or not an unpaired electron is spin polarized. Significantly, our calculations even suggest the existence of the intrinsic Ising superconductor in metallic α_1 -TaSi₂N₄ monolayer material. It is mainly because that superconductive cooper pairs formed from carriers in intrinsic spin-orbit coupling valleys at K and K' points exhibit locked opposite spins. This behavior implies that its superconductivity has no responsibility to an in-plane pair-breaking field such as magnetic field, which can remarkably enhance its in-plane upper critical field.

Finally, we would like to emphasize that our currently proposed intercalated architecture approach can be indeed extended to MA_2Z_4 monolayer materials with M for late transition metal elements, such as MnBi₂Te₄ for which our current

calculations also correctly capture the agreements to experiments. Furthermore, it can be further generalized to a wider way. For instance, $n=7$ MA_2Z_4 monolayer materials can be also constructed by intercalating $n = 2$ germanene monolayer into $n=5$ vdW Bi_2Se_3 monolayer structure and, we can even combine $n=3$ MoS_2 monolayer materials and $n=5$ vdW Bi_2Se_3 monolayer structure to form new type of $n=8$ monolayer materials, and so on.

III. METHOD

Electronic and phononic band structures. First-principles calculations were employed using the Vienna *ab initio* simulation package (VASP)^{58,59} with the exchange-correlation (XC) potential of Perdew-Burke-Ernzerhof (PBE) type and projector augmented wave (PAW) method. Since the transition metal element M in MA_2Z_4 monolayer have a larger atomic mass, we also considered the spin-orbit coupling (SOC) to calculate electronic band structure. Furthermore, in order to get more exact bandgap, hybrid Heyd-Scuseria-Ernzerhof (HSE06) functionals are also employed. Taken all the elements into consideration, the 500 eV cutoff energy was chose. And the k -point sampling grid in the self-consistent process was $15 \times 15 \times 1$ in Γ -centered Monkhorst-Pack scheme. The Force convergence criteria on each atom is less than 10^{-3} eV/Å and the energy convergence criteria on the primitive cell is less 10^{-6} eV. To minimize the interactions between the layer with its periodic images, a vacuum of 20 Å between layers was considered.

Phonon spectra was obtained using the density functional perturbation theory (DFPT) method implemented in Phonopy⁶⁰ package. $4 \times 4 \times 1$ and $5 \times 5 \times 1$ supercell are used for the calculation of the phonon spectra to make sure that the force constants are sufficiently collected. In addition, we applied an iterative Green functions method⁶¹ to calculate the edge states and used the Wannier charge centers method introduced in Ref. 62 to obtain the Z_2 value.

Electron-phonon coupling and superconductivity. For metallic materials, the electron-phonon coupling (EPC) constant $\lambda(\omega)$ ⁶³ is given by

$$\lambda(\omega) = 2 \int d\omega \alpha^2 F(\omega) / \omega \quad (1)$$

where $\alpha^2 F(\omega)$ is the Eliashberg function and defined as

$$\alpha^2 F(\omega) = \frac{1}{2\pi N(\epsilon_F)} \sum_{q\nu} \delta(\omega - \omega_{q\nu}) \frac{\gamma_{q\nu}}{\hbar\omega_{q\nu}} \quad (2)$$

where $N(\epsilon_F)$ is density of states (DOS) at Fermi level, $\omega_{q\nu}$ is phonon frequency of the mode ν at the wavevector \mathbf{q} and $\gamma_{q\nu}$ is phonon linewidth or lifetime.

Based on BCS theory, the results of Eliashberg function $\alpha^2 F(\omega)$ can be used to calculate logarithmic average phonon frequencies by $\omega_{\log} = \exp \left[\frac{2}{\lambda} \int_0^\infty \frac{d\omega}{\omega} \alpha^2 F(\omega) \log \omega \right]$ and, further, to calculate the superconductivity critical temperature,

$T_c = \frac{\omega_{\log}}{1.2} \exp \left[\frac{-1.04(1+\lambda)}{\lambda - \mu^*(1+0.62\lambda)} \right]$, by using the simple Allen-Dynes-modified McMillan formula⁶⁴.

The EPC in this work calculated with local density approximation⁶⁵ as implemented in the Quantum-ESPRESSO⁶⁶ package with Norm-conserving pseudopotentials (NCPP). For α_1 - $TaSi_2N_4$ and β_2 - $HfGe_2P_4$, the kinetic energy cutoff and the charge density cutoff of the plane wave basis are chosen to be 60 and 480 Ry. $32 \times 32 \times 1$ k-mesh with Marzari-Vanderbilt cold smearing of 0.02 Ry is used to evaluate the self-consistent electron density. $4 \times 4 \times 1$ q-mesh are used to obtain the dynamic matrix and EPC constant, respectively. For α_2 - $TaGe_2P_4$, due to the softening of its acoustic mode, 80 Ry kinetic energy cutoff, 640 Ry charge density cutoff, $36 \times 36 \times 1$ k-mesh, $6 \times 6 \times 1$ q-mesh are used to calculate its EPC strength and its T_c .

Carrier mobilities. Intrinsic carrier mobility μ of 2D materials based on deformation potential is calculated by⁶⁷

$$\mu_{2D} = \frac{2e\hbar^3 C}{3k_B T |m^*|^2 E_1^2} \quad (3)$$

where C is the elastic modulus defined as $[\partial^2 E / \partial \delta^2] / S_0$, m^* is the effective mass at conduction band minimum (CBM) or valance band maximum (VBM), and T is the temperature, here room temperature $T = 300$ K was used. E_1 is the deformation potential (DP) constant defined as $\Delta E / (\Delta l / l_0)$, where ΔE is the change of the eigenvalue at CBM or VBM and Δl is the lattice dilation along deformation direction.

Enthalpies of formation. Enthalpies of formation (E_f) per atom can be expressed by the following equation:

$$E_f = \{E_{tot} - (E_M + 2E_A + 4E_Z)\} / 7 \quad (4)$$

Where E_{tot} is the total energy of the system, and E_M , E_A and E_Z are the ground state energies of elementary substances M , A and Z in MA_2X_4 compounds, respectively.

Berry curvature calculation. The Berry curvature of a 2D material with n bands can be defined as^{68,69}:

$$\Omega_z(\mathbf{k}) = \nabla_{\mathbf{k}} \times i \langle u_{n,\mathbf{k}} | \nabla_{\mathbf{k}} u_{n,\mathbf{k}} \rangle \quad (5)$$

where $u_{n,\mathbf{k}}$ is the lattice periodic part of the Bloch wave functions. And it can be derived by a tight binding Hamiltonian obtained from first principle calculations via maximally-localized Wannier functions method⁷⁰. Here, we used all occupied bands and the approach introduced by Ref. 71 to calculate the Berry curvature.

IV. ACKNOWLEDGMENTS

Work was supported by the National Science Fund for Distinguished Young Scholars (grant number 51725103), by the National Natural Science Foundation of China (grant number 51671193), by the Science Challenging Project (grant number TZ2016004), and by major research project 2018ZX06002004. M.C. was supported by the National Natural Science Foundation of China (Grant No. 11774084) and

the Project of Educational Commission of Hunan Province of China, 18A003. All calculations have been performed on the high-performance computational cluster in the Shenyang National University Science and Technology Park.

V. AUTHOR CONTRIBUTIONS

X.-Q.C. supervised this project. Structural model and structural optimization as well as band structure calculations were performed by L.W.. Y.S. and Q.G. carried out theoretical calculations of carrier mobility and M.L. and R.L. performed

detailed calculations of electron-phonon coupling. L.W. and X.-Q. C. wrote the manuscript with contributions from all authors. All authors including Y.-L.H, W.R. ,M.C. ,H.-M.C. and Y.L. discussed the results and commented on the manuscript.

VI. DECLARATION OF INTERESTS

The authors declare no competing financial interests.

VII. REFERENCES

-
- * xingqiu.chen@imr.ac.cn
- ¹ F. Bonaccorso, L. Colombo, G. Yu, M. Stoller, V. Tozzini, A. C. Ferrari, R. S. Ruoff, and V. Pellegrini, *Science* **347** (2015).
 - ² R. Raccichini, A. Varzi, S. Passerini, and B. Scrosati, *Nature Mater* **14**, 271 (2015).
 - ³ D. Akinwande, N. Petrone, and J. Hone, *Nature Communications* **5**, 1 (2014).
 - ⁴ H.-Y. Chang, M. N. Yogeesh, R. Ghosh, A. Rai, A. Sanne, S. Yang, N. Lu, S. K. Banerjee, and D. Akinwande, *Advanced Materials* **28**, 1818 (2016).
 - ⁵ D. Xiao, G.-B. Liu, W. Feng, X. Xu, and W. Yao, *Phys. Rev. Lett.* **108**, 196802 (2012).
 - ⁶ D. Pesin and A. H. MacDonald, *Nature Materials* **11**, 409 (2012).
 - ⁷ C. Wang, B. Lian, X. Guo, J. Mao, Z. Zhang, D. Zhang, B.-L. Gu, Y. Xu, and W. Duan, *Phys. Rev. Lett.* **123**, 126402 (2019).
 - ⁸ J. M. Lu, O. Zheliuk, I. Leermakers, N. F. Q. Yuan, U. Zeitler, K. T. Law, and J. T. Ye, *Science* **350**, 1353 (2015).
 - ⁹ B. T. Zhou, N. F. Q. Yuan, H.-L. Jiang, and K. T. Law, *Physical Review B* **93**, 180501(R) (2016).
 - ¹⁰ Y. Saito, Y. Nakamura, M. S. Bahramy, Y. Kohama, J. Ye, Y. Kasahara, Y. Nakagawa, M. Onga, M. Tokunaga, T. Nojima, Y. Yanase, and Y. Iwasa, *Nature Physics* **12**, 144 (2016).
 - ¹¹ Y. Liu, Z. Wang, X. Zhang, C. Liu, Y. Liu, Z. Zhou, J. Wang, Q. Wang, Y. Liu, C. Xi, M. Tian, H. Liu, J. Feng, X. C. Xie, and J. Wang, *Phys. Rev. X* **8**, 021002 (2018).
 - ¹² X. Xi, Z. Wang, W. Zhao, J.-H. Park, K. T. Law, H. Berger, L. Forr, J. Shan, and K. F. Mak, *Nature Physics* **12**, 139 (2016).
 - ¹³ S. C. de la Barrera, M. R. Sinko, D. P. Gopalan, N. Sivadas, K. L. Seyler, K. Watanabe, T. Taniguchi, A. W. Tsun, X. Xu, D. Xiao, and B. M. Hunt, *Nature Communications* **9**, 1427 (2018).
 - ¹⁴ J. Falson, Y. Xu, M. Liao, Y. Zang, K. Zhu, C. Wang, Z. Zhang, H. Liu, W. Duan, K. He, H. Liu, J. H. Smet, D. Zhang, and Q.-K. Xue, *Science* **367**, 1454 (2020).
 - ¹⁵ G. Profeta, M. Calandra, and F. Mauri, *Nature Physics* **8**, 131 (2012).
 - ¹⁶ C. Si, Z. Liu, W. Duan, and F. Liu, *Physical Review Letters* **111**, 196802 (2013).
 - ¹⁷ L. Banszerus, M. Schmitz, S. Engels, J. Dauber, M. Oellers, F. Haupt, K. Watanabe, T. Taniguchi, B. Beschoten, and C. Stampfer, *Science Advances* **1**, e1500222 (2015).
 - ¹⁸ C. Lee, X. Wei, J. W. Kysar, and J. Hone, *Science* **321**, 385 (2008).
 - ¹⁹ E. Pop, V. Varshney, and A. K. Roy, *MRS Bull.* **37**, 1273 (2012).
 - ²⁰ D.E. Sheehy and J. Schmalian, *Phys. Rev. B* **80**, 193411 (2009).
 - ²¹ A.B. Kuzmenko, E. vanHeumen, F. Carbone and D.vanderMarel, *Phys. Rev. Lett.* **100**, 117401 (2008).
 - ²² K. Watanabe, T. Taniguchi, and H. Kanda, *Nature Materials* **3**, 404 (2004).
 - ²³ L. Song, L. Ci, H. Lu, P. B. Sorokin, C. Jin, J. Ni, A. G. Kvasninin, D. G. Kvasninin, J. Lou, B. I. Yakobson, and P. M. Ajayan, *Nano Lett.* **10**, 3209 (2010).
 - ²⁴ K. F. Mak, C. Lee, J. Hone, J. Shan, and T. F. Heinz, *Phys. Rev. Lett.* **105**, 136805 (2010).
 - ²⁵ Q. H. Wang, K. Kalantar-Zadeh, A. Kis, J. N. Coleman, and M. S. Strano, *Nature Nanotechnology* **7**, 699 (2012).
 - ²⁶ A. A. Soluyanov, D. Gresch, Z. Wang, Q. Wu, M. Troyer, X. Dai, and B. A. Bernevig, *Nature* **527**, 495 (2015).
 - ²⁷ P. Li, Y. Wen, X. He, Q. Zhang, C. Xia, Z.-M. Yu, S. A. Yang, Z. Zhu, H. N. Alshareef, and X.-X. Zhang, *Nature Communications* **8**, 1 (2017).
 - ²⁸ A. Eftekhari, *J. Mater. Chem. A* **5**, 18299 (2017).
 - ²⁹ H. Xiang, B. Xu, J. Liu, Y. Xia, H. Lu, J. Yin, and Z. Liu, *AIP Advances* **6**, 095005 (2016).
 - ³⁰ S. Jiang, L. Li, Z. Wang, K. F. Mak, and J. Shan, *Nature nanotechnology* **13**, 549 (2018).
 - ³¹ B. Huang, G. Clark, D. R. Klein, D. MacNeill, E. Navarro-Moratalla, K. L. Seyler, N. Wilson, M. A. McGuire, D. H. Cobden, D. Xiao, et al., *Nature nanotechnology* **13**, 544 (2018).
 - ³² Z. Wang, I. Gutiérrez-Lezama, N. Ubrig, M. Kroner, M. Gibertini, T. Taniguchi, K. Watanabe, A. Imamoglu, E. Giannini, and A. F. Morpurgo, *Nature communications* **9**, 1 (2018).
 - ³³ W. Li and J. Li, *Nano Research* **8**, 3796 (2015).
 - ³⁴ H. L. Zhuang and R. G. Hennig, *Chem. Mater.* **25**, 3232 (2013).
 - ³⁵ Y. Sun, S. Luo, X.-G. Zhao, K. Biswas, S.-L. Li, and L. Zhang, *Nanoscale* **10**, 7991 (2018).
 - ³⁶ A. V. Lugovskoi, M. I. Katsnelson, and A. N. Rudenko, *Physical Review Letters* **123**, 176401 (2019).
 - ³⁷ H. Zhang, C.-X. Liu, X.-L. Qi, X. Dai, Z. Fang, and S.-C. Zhang, *Nature Physics* **5**, 438 (2009).
 - ³⁸ D. Hsieh, Y. Xia, D. Qian, L. Wray, J. H. Dil, F. Meier, J. Osterwalder, L. Patthey, J. G. Checkelsky, N. P. Ong, A. V. Fedorov, H. Lin, A. Bansil, D. Grauer, Y. S. Hor, R. J. Cava, and M. Z. Hasan, *Nature* **460**, 1101 (2009).
 - ³⁹ C. Gong, L. Li, Z. Li, H. Ji, A. Stern, Y. Xia, T. Cao, W. Bao, C. Wang, Y. Wang, et al., *Nature* **546**, 265 (2017).
 - ⁴⁰ J. Zhou, L. Shen, M. D. Costa, K. A. Persson, S. P. Ong, P. Huck, Y. Lu, X. Ma, Y. Chen, H. Tang, and Y. P. Feng, *Scientific Data* **6**, 1 (2019).
 - ⁴¹ D. Zhang, M. Shi, T. Zhu, D. Xing, H. Zhang, and J. Wang, *Phys. Rev. Lett.* **122**, 206401 (2019).

- ⁴² J. Li, Y. Li, S. Du, Z. Wang, B.-L. Gu, S.-C. Zhang, K. He, W. Duan, and Y. Xu, *Science Advances* **5**, eaaw5685 (2019).
- ⁴³ M. M. Otrokov, I. I. Klimovskikh, H. Bentmann, D. Estyunin, A. Zeugner, Z. S. Aliev, S. GaSS, A. U. B. Wolter, A. V. Koroleva, A. M. Shikin, M. Blanco-Rey, M. Hoffmann, I. P. Rusinov, A. Y. Vyazovskaya, S. V. Ereemeev, Y. M. Koroteev, V. M. Kuznetsov, F. Freyse, J. Sánchez-Barriga, I. R. Amiraslanov, M. B. Babanly, N. T. Mamedov, N. A. Abdullayev, V. N. Zverev, A. Alfonsov, V. Kataev, B. Büchner, E. F. Schwier, S. Kumar, A. Kimura, L. Petaccia, G. Di Santo, R. C. Vidal, S. Schatz, K. KiSSner, M. Uüzelmann, C. H. Min, S. Moser, T. R. F. Peixoto, F. Reinert, A. Ernst, P. M. Echenique, A. Isaeva, and E. V. Chulkov, *Nature* **576**, 416 (2019).
- ⁴⁴ E. D. L. Rienks, S. Wimmer, J. Sánchez-Barriga, O. Caha, P. S. Mandal, J. Røuzička, A. Ney, H. Steiner, V. V. Volobuev, H. Groiss, M. Albu, G. Kothleitner, J. Michalička, S. A. Khan, J. Minar, H. Ebert, G. Bauer, F. Freyse, A. Varykhalov, O. Rader, and G. Springholz, *Nature* **576**, 423 (2019).
- ⁴⁵ Y. Deng, Y. Yu, M. Z. Shi, Z. Guo, Z. Xu, J. Wang, X. H. Chen, and Y. Zhang, *Science* **367**, 895 (2020).
- ⁴⁶ Y.-L. Hong, Z. Liu, L. Wang, T. Zhou, W. Ma, C. Xu, S. Feng, L. Chen, M.-L. Chen, D.-M. Sun, X.-Q. Chen, H.-M. Cheng, and W. Ren, *Science*, **369**, 670–674 (2020).
- ⁴⁷ B. Özdamar, G. Özbal, M. N. Çınar, K. Sevim, G. Kurt, B. Kaya, and H. Sevinçli, *Phys. Rev. B* **98**, 045431 (2018).
- ⁴⁸ Supplementary materials contain (i) seven supplementary figures S1 to S8, and (ii) four supplementary Tables S1 to S4.
- ⁴⁹ D. Xiao, G.-B. Liu, W. Feng, X. Xu, and W. Yao, *Physical Review Letters* **108**, 196802 (2012).
- ⁵⁰ A. M. Jones, H. Yu, J. S. Ross, P. Klement, N. J. Ghimire, J. Yan, D. G. Mandrus, W. Yao, and X. Xu, *Nature Physics* **10**, 130 (2014).
- ⁵¹ A. M. Jones, H. Yu, N. J. Ghimire, S. Wu, G. Aivazian, J. S. Ross, B. Zhao, J. Yan, D. G. Mandrus, D. Xiao, W. Yao, and X. Xu, *Nature Nanotechnology* **8**, 634 (2013).
- ⁵² D. Xiao, W. Yao, and Q. Niu, *Physical Review Letters* **99**, 236809 (2007).
- ⁵³ W. Yao, D. Xiao, and Q. Niu, *Physical Review B* **77**, 235406 (2008).
- ⁵⁴ A. Allain and A. Kis, *ACS Nano* **8**, 7180 (2014).
- ⁵⁵ A. Rawat, N. Jena, Dimple, and A. D. Sarkar, *Journal of Materials Chemistry A* **6**, 8693 (2018).
- ⁵⁶ X. L. Wang, *Physical Review Letters* **100**, 156404 (2008).
- ⁵⁷ X. Wang, *National Science Review* **4**, 252 (2017).
- ⁵⁸ G. Kresse and J. Furthmüller, *Physical Review B* **54**, 11169 (1996).
- ⁵⁹ G. Kresse and D. Joubert, *Physical Review B* **59**, 1758 (1999).
- ⁶⁰ A. Togo and I. Tanaka, *Scripta Materialia* **108**, 1 (2015).
- ⁶¹ M. P. L. Sancho, J. M. L. Sancho, and J. Rubio, *J. Phys. F* **15**, 851 (1985).
- ⁶² A.A. Soluyanov, D. Vanderbilt, *Phys. Rev. B* **83**, 235401 (2011).
- ⁶³ G. Eliashberg, *Sov. Phys. - JETP (Engl. Transl.)*; (United States) **11:3** (1960).
- ⁶⁴ P. B. Allen and R. C. Dynes, *Physical Review B* **12**, 905 (1975).
- ⁶⁵ J. P. Perdew and A. Zunger, *Phys. Rev. B* **23**, 5048 (1981).
- ⁶⁶ P. Giannozzi, S. Baroni, N. Bonini, M. Calandra, R. Car, C. Cavazzoni, D. Ceresoli, G. L. Chiarotti, M. Cococcioni, I. Dabo, A. D. Corso, S. d. Gironcoli, S. Fabris, G. Fratesi, R. Gebauer, U. Gerstmann, C. Gougoussis, A. Kokalj, M. Lazzeri, L. Martin-Samos, N. Marzari, F. Mauri, R. Mazzarello, S. Paolini, A. Pasquarello, L. Paulatto, C. Sbraccia, S. Scandolo, G. Sclauzero, A. P. Seitsonen, A. Smogunov, P. Umari, and R. M. Wentzcovitch, *Journal of Physics: Condensed Matter* **21**, 395502 (2009).
- ⁶⁷ J. Bardeen and W. Shockley, *Phys. Rev.* **80**, 72 (1950).
- ⁶⁸ D. Xiao, M.-C. Chang, and Q. Niu, *Reviews of Modern Physics* **82**, 1959 (2010).
- ⁶⁹ A. Kormányos, V. Zlyomi, V. I. Falko, and G. Burkard, *Physical Review B* **98**, 035408 (2018).
- ⁷⁰ N. Marzari and D. Vanderbilt, *Phys. Rev. B* **56**, 12847 (1997).
- ⁷¹ X. Wang, J. R. Yates, I. Souza, and D. Vanderbilt, *Physical Review B* **74**, 195118 (2006).
- ⁷² Y. Cai, G. Zhang, and Y.-W. Zhang, *J. Am. Chem. Soc.* **136**, 6269 (2014).

Supplementary Materials including as follows,

**1) Supplementary Figures S1 (page 11) to S8
(page 17)**

**2) Supplementary Tables S1 (page 19) to S4
(page 22)**

32 valence electrons

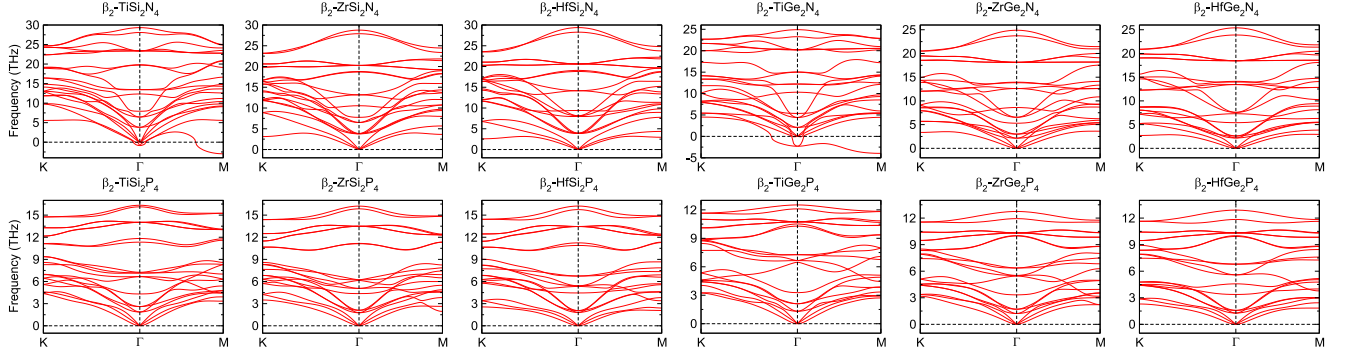
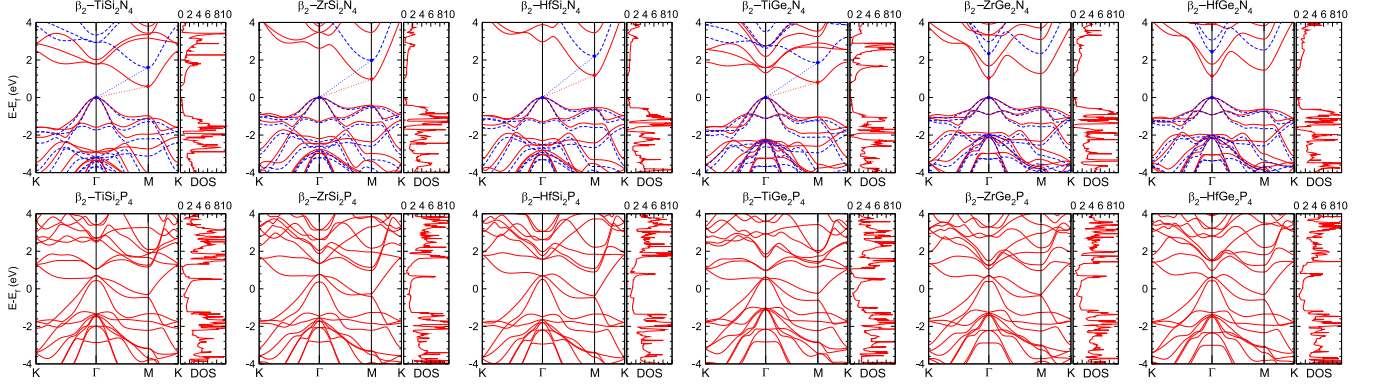
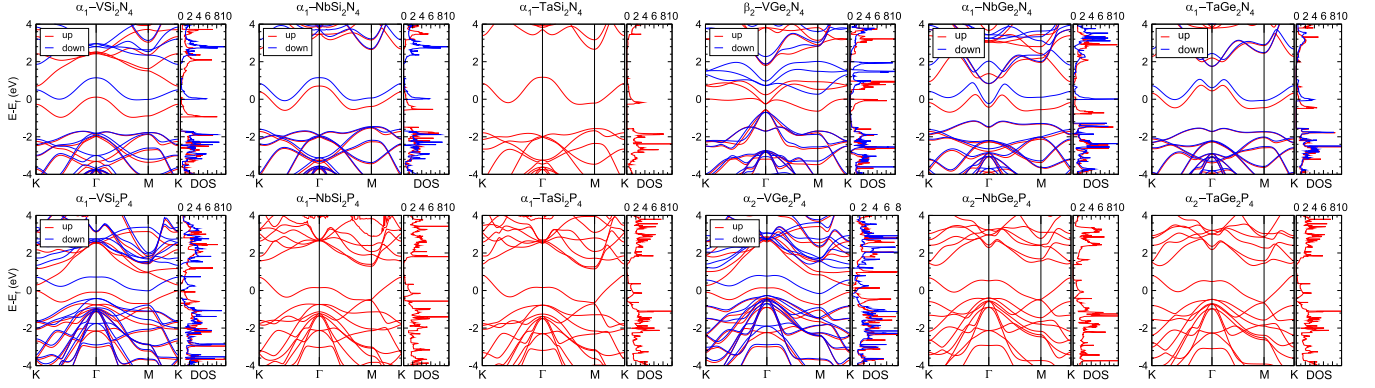


Fig. S1, The phonon spectrum of 36 septuple-atomic-layer MA_2Z_4 monolayers listed in Table S2.

32 valence electrons



33 valence electrons



34 valence electrons

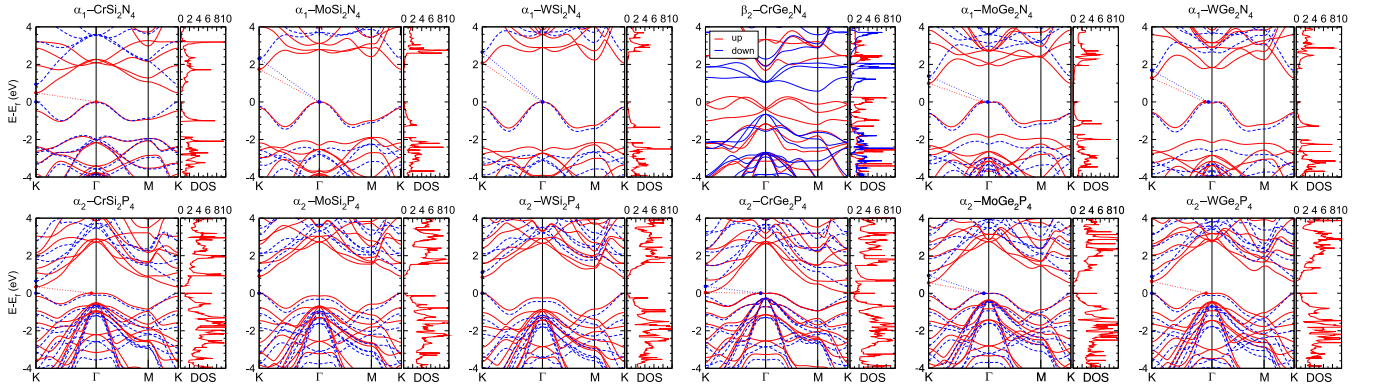


Fig. S2, (color online) The electronic structures of 36 septuple-layer MA_2Z_4 monolayers listed in [Table S2](#), where, for semiconductors, the red solid and blue dash bands are calculated by PBE and HSE06 functional without inclusion of spin orbit coupling (SOC) and, for ferromagnetic metallic compounds, the red and blue solid bands represent spin up and spin down bands.

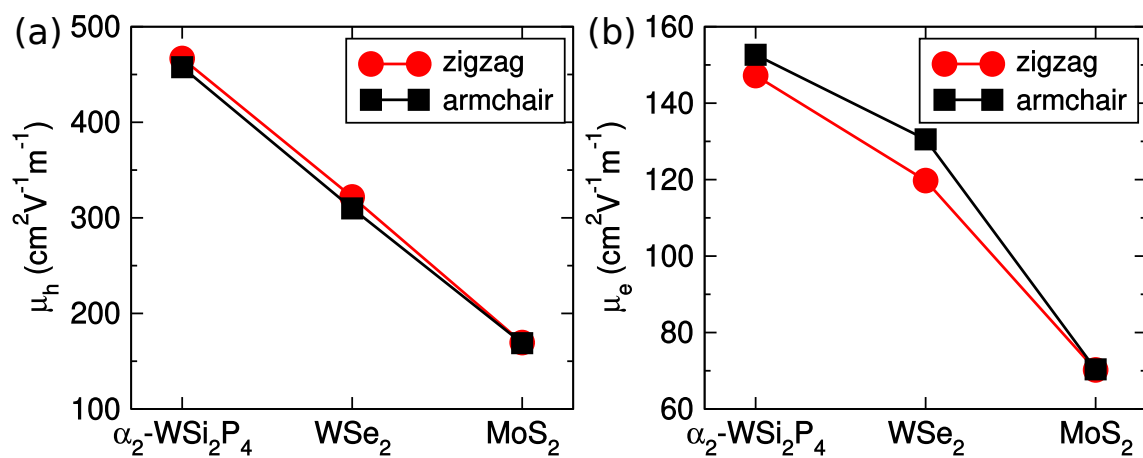


Fig. S3, (color online) Hole and electron mobility of α_2 -WSi₂P₄, WSe₂ and MoS₂. Note that all the detail data used to calculate hole and electron mobility are listed in [Table S4](#)

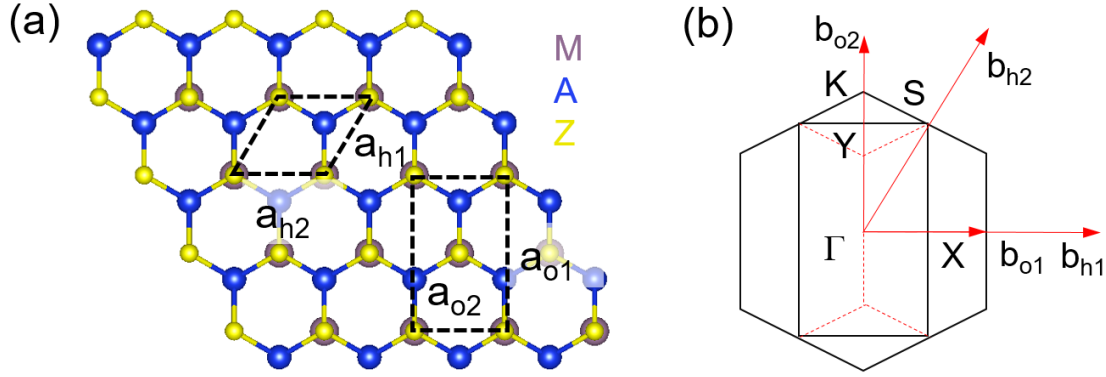


Fig. S4, (color online) (a) The top view of α_2 - MA_2Z_4 monolayer. The dashed black lines represent the hexagonal primitive cell and orthogonal supercell. (b) The FBZ of these two lattices. The dashed red line shows the folding of FBZ of hexagonal cell into FBZ of orthogonal cell.

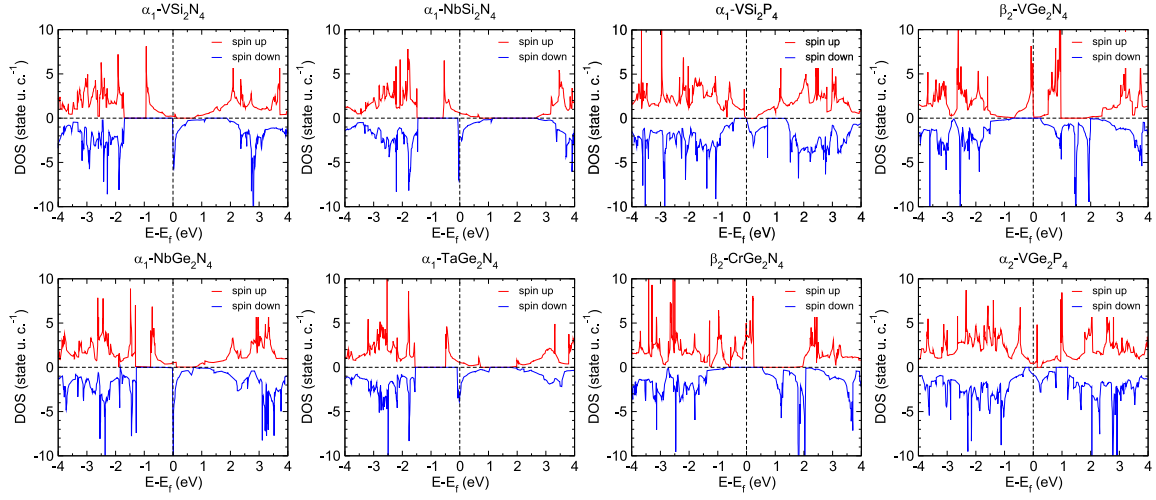


Fig. S5, (color online) The DOS of eight ferromagnetic MA_2Z_4 monolayers.

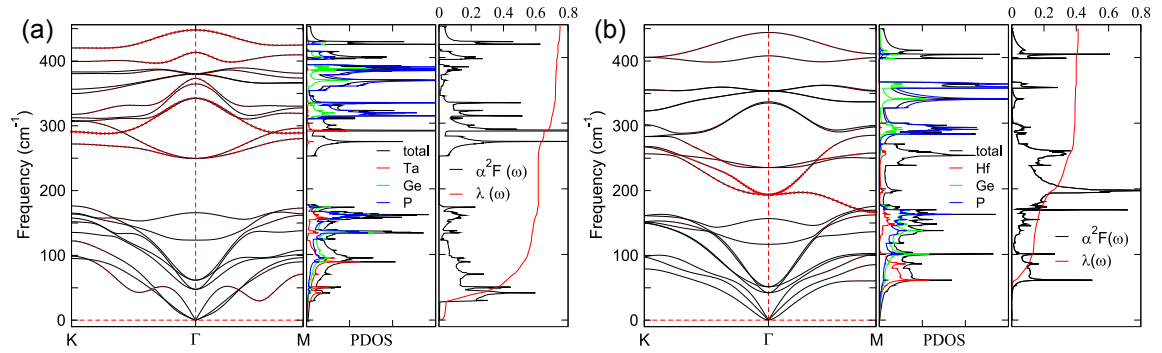


Fig. S6, (color online) The phonon dispersion, phonon DOS and Eliashberg function $\alpha^2 F(\omega)$ with EPC strength $\lambda(\omega)$ of the α_2 -TaGe₂P₄ (a) and β_2 -HfGe₂P₄ (b), where the area of the red circles represents the strength of phonon linewidth $\gamma_{q,\nu}$,

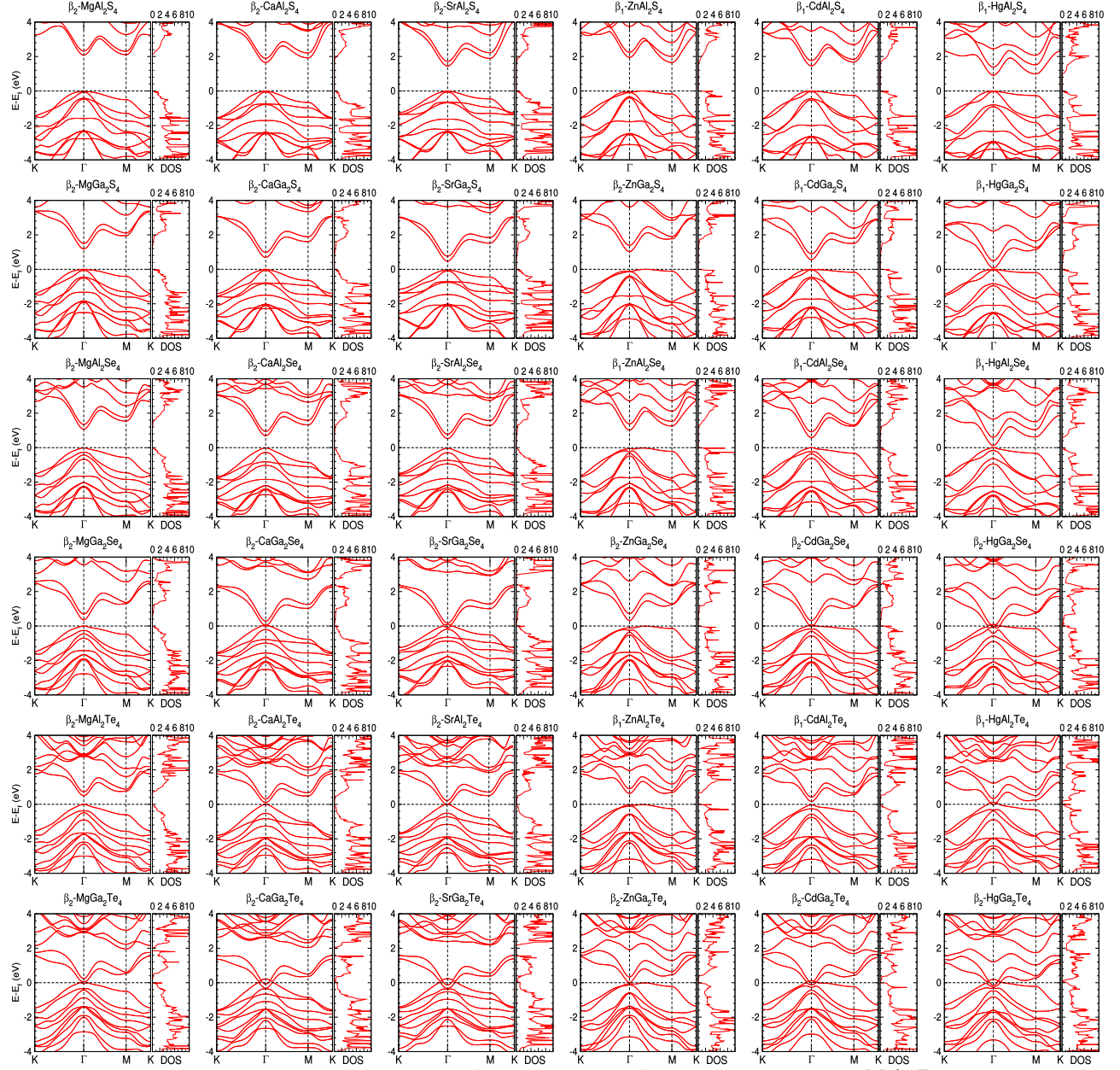


Fig. S7, (color online) The electronic structures of 36 energetically favorable septuple-layer MA_2Z_4 monolayers, as listed in [Table S3](#), with inclusion of spin orbit coupling.

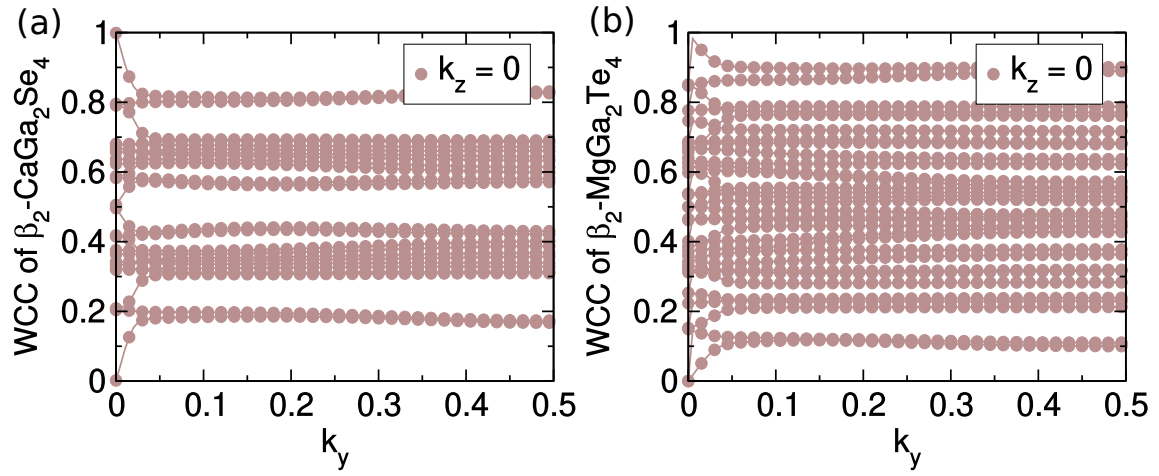


Fig. S8, (color online) Evolution of Wannier charge center (WCC) of β_2 -CaGa₂Se₄ (a) and β_2 -MgGa₂Te₄ (b) in the $k_z = 0$ plane, which implies a nonzero topological invariant.

Table S1, The enthalpies of formation E_f (eV/atom) of α_{1-6} - and β_{1-6} - MA_2Z_4 monolayers with space group $P\bar{6}m2$ and $P\bar{3}m1$, respectively, where $M = \text{Ti, Zr, Hf, V, Nb, Ta, Cr, Mo, W}$; $A = \text{Si and Ge}$; $Z = \text{N and P}$.

No.	Name	α_1	α_2	α_3	α_4	α_5	α_6	β_1	β_2	β_3	β_4	β_5	β_6
01	TiSi ₂ N ₄	-1.052	-1.036	-0.262	-0.633	-0.668	-0.282	-1.091	-1.119	-0.765	-0.405	-0.708	-0.369
02	ZrSi ₂ N ₄	-0.991	-0.986	-0.183	-0.558	-0.570	-0.196	-1.013	-1.028	-0.631	-0.272	-0.595	-0.235
03	HfSi ₂ N ₄	-1.053	-1.047	-0.217	-0.602	-0.617	-0.231	-1.091	-1.105	-0.694	-0.333	-0.661	-0.298
04	TiGe ₂ N ₄	-0.331	-0.326	0.242	-0.009	-0.021	0.087	-0.395	-0.409	-0.142	0.083	-0.105	0.115
05	ZrGe ₂ N ₄	-0.378	-0.376	0.220	-0.040	-0.039	0.221	-0.426	-0.433	-0.133	0.098	-0.113	0.128
06	HfGe ₂ N ₄	-0.425	-0.423	0.193	-0.073	-0.074	0.195	-0.489	-0.496	-0.183	0.051	-0.165	0.077
07	TiSi ₂ P ₄	-0.327	-0.316	0.171	-0.034	-0.204	-0.101	-0.335	-0.348	-0.193	-0.010	-0.073	0.075
08	ZrSi ₂ P ₄	-0.366	-0.349	0.080	-0.077	-0.206	-0.129	-0.372	-0.390	-0.252	-0.074	-0.114	0.043
09	HfSi ₂ P ₄	-0.357	-0.342	0.122	-0.060	-0.155	-0.095	-0.366	-0.383	-0.231	-0.048	-0.104	0.049
10	TiGe ₂ P ₄	-0.194	-0.190	0.153	0.020	-0.117	-0.018	-0.196	-0.200	-0.011	0.004	0.051	0.123
11	ZrGe ₂ P ₄	-0.253	-0.244	0.023	0.017	-0.127	-0.132	-0.253	-0.262	-0.096	-0.096	-0.013	0.077
12	HfGe ₂ P ₄	-0.243	-0.235	0.066	0.026	-0.106	-0.091	-0.249	-0.258	-0.076	-0.070	-0.006	0.083
13	VSi ₂ N ₄	-0.954	-0.933	-0.196	-0.545	-0.619	-0.231	-0.913	-0.949	-0.637	-0.252	-0.540	-0.211
14	NbSi ₂ N ₄	-0.989	-0.964	-0.206	-0.552	-0.628	-0.245	-0.927	-0.966	-0.629	-0.243	-0.534	-0.206
15	TaSi ₂ N ₄	-1.009	-0.978	-0.205	-0.551	-0.634	-0.244	-0.944	-0.984	-0.633	-0.252	-0.537	-0.222
16	VGe ₂ N ₄	-0.173	-0.167	0.359	0.138	0.098	0.320	-0.171	-0.186	0.057	0.280	0.123	0.312
17	NbGe ₂ N ₄	-0.293	-0.280	0.254	0.036	-0.016	0.222	-0.255	-0.275	-0.029	0.173	0.042	0.186
18	TaGe ₂ N ₄	-0.310	-0.295	0.238	0.031	-0.027	0.214	-0.276	-0.298	-0.043	0.134	0.028	0.144
19	VSi ₂ P ₄	-0.246	-0.244	0.112	0.026	-0.111	0.023	-0.221	-0.225	-0.061	0.127	0.009	0.157
20	NbSi ₂ P ₄	-0.321	-0.317	0.210	-0.049	-0.156	0.005	-0.290	-0.294	-0.138	0.087	-0.065	0.081
21	TaSi ₂ P ₄	-0.297	-0.293	0.256	-0.025	-0.113	0.050	-0.270	-0.270	-0.101	0.123	-0.048	0.095
22	VGe ₂ P ₄	-0.091	-0.098	0.130	0.117	0.011	0.059	-0.069	-0.063	0.114	0.142	0.145	0.228
23	NbGe ₂ P ₄	-0.176	-0.183	0.211	0.060	-0.028	0.019	-0.151	-0.139	0.053	0.105	0.053	0.142
24	TaGe ₂ P ₄	-0.153	-0.161	0.258	0.081	0.017	0.069	-0.131	-0.122	0.078	0.140	0.064	0.153
25	CrSi ₂ N ₄	-0.831	-0.807	-0.082	-0.429	-0.512	-0.119	-0.731	-0.762	-0.458	-0.037	0.106	-0.014
26	MoSi ₂ N ₄	-0.955	-0.931	-0.157	-0.517	-0.591	-0.189	-0.775	-0.803	-0.470	-0.057	-0.388	-0.052
27	WSi ₂ N ₄	-0.955	-0.929	-0.147	-0.502	-0.579	-0.177	-0.757	-0.782	-0.434	-0.033	-0.363	-0.042
28	CrGe ₂ N ₄	0.004	0.009	0.514	0.299	0.242	0.479	-0.001	-0.014	0.263	0.479	0.308	0.505
29	MoGe ₂ N ₄	-0.185	-0.177	0.355	0.136	0.082	0.327	-0.044	-0.056	0.187	0.410	0.249	0.427
30	WGe ₂ N ₄	-0.187	-0.178	0.352	0.144	0.088	0.327	-0.030	-0.042	0.205	0.393	0.266	0.408
31	CrSi ₂ P ₄	-0.176	-0.184	0.186	0.082	-0.022	0.145	-0.122	-0.149	0.022	0.145	0.092	0.255
32	MoSi ₂ P ₄	-0.294	-0.303	0.137	-0.030	-0.050	0.141	-0.210	-0.202	0.003	0.183	-0.003	0.141
33	WSi ₂ P ₄	-0.241	-0.252	0.185	0.021	0.022	0.210	-0.159	-0.146	0.070	0.259	0.051	0.192
34	CrGe ₂ P ₄	0.001	-0.015	0.219	0.197	0.118	0.187	-0.006	-0.006	0.152	0.194	0.230	0.305
35	MoGe ₂ P ₄	-0.127	-0.144	0.348	0.105	0.087	0.163	-0.052	-0.036	0.197	0.197	0.126	0.203
36	WGe ₂ P ₄	-0.077	-0.094	0.423	0.152	0.168	0.238	-0.005	0.013	0.259	0.276	0.175	0.249

Table S2, Structural and electronic properties of 36 MA_2Z_4 monolayers with three energetically favorable phases (α_1 -, α_2 - and β_2 -phase) extracted from **Table S1**. Lattice constant (a), bond length (d_{A-Z}^v , d_{Z-M} and d_{A-Z}^h , where v or h represents the bond along vertical or horizontal direction), band gap calculated with PBE and HSE06 XC functionals (E_g^{PBE} and E_g^{HSE06}), respectively, magnets μ_B , the type of energetic favorable phase and dynamical stability, where VEC is the number of valence electrons of primitive cell of MA_2Z_4 monolayers

VEC	No.	Name	a (Å)	d_{A-Z}^v (Å)	d_{Z-M} (Å)	d_{A-Z}^h (Å)	E_g^{PBE} (eV)	E_g^{HSE06} (eV)	mag (μ_B)	Phase	Dynamics (Y/N)
32 VEC	01	TiSi ₂ N ₄	2.95	1.77	2.04	1.75	0.61(Γ -M)	1.60(Γ -M)	—	β_2	N
	02	ZrSi ₂ N ₄	3.05	1.83	2.16	1.75	1.00(Γ -M)	1.98(Γ -M)	—	β_2	Y
	03	HfSi ₂ N ₄	3.04	1.82	2.14	1.75	1.21(Γ -M)	2.21(Γ -M)	—	β_2	Y
	04	TiGe ₂ N ₄	3.08	1.89	2.08	1.89	0.82(Γ -M)	1.86(Γ -M)	—	β_2	N
	05	ZrGe ₂ N ₄	3.19	1.93	2.19	1.89	1.04(Γ - Γ)	2.34(Γ - Γ)	—	β_2	Y
	06	HfGe ₂ N ₄	3.18	1.93	2.17	1.89	1.15(Γ - Γ)	2.45(Γ - Γ)	—	β_2	Y
	07	TiSi ₂ P ₄	3.53	2.27	2.49	2.22	—	—	—	β_2	Y
	08	ZrSi ₂ P ₄	3.61	2.30	2.61	2.22	—	—	—	β_2	Y
	09	HfSi ₂ P ₄	3.61	2.30	2.59	2.22	—	—	—	β_2	Y
	10	TiGe ₂ P ₄	3.64	2.36	2.51	2.32	—	—	—	β_2	Y
	11	ZrGe ₂ P ₄	3.72	2.38	2.63	2.32	—	—	—	β_2	Y
	12	HfGe ₂ P ₄	3.72	2.38	2.60	2.33	—	—	—	β_2	Y
33 VEC	13	VSi ₂ N ₄	2.88	1.75	2.03	1.75	—	—	0.97	α_1	Y
	14	NbSi ₂ N ₄	2.96	1.78	2.13	1.75	—	—	0.57	α_1	Y
	15	TaSi ₂ N ₄	2.97	1.78	2.13	1.75	—	—	—	α_1	Y
	16	VGe ₂ N ₄	3.05	1.87	2.06	1.89	—	—	0.98	β_2	N
	17	NbGe ₂ N ₄	3.09	1.89	2.16	1.90	—	—	0.72	α_1	Y
	18	TaGe ₂ N ₄	3.08	1.87	2.15	1.88	—	—	0.49	α_1	Y
	19	VSi ₂ P ₄	3.48	2.25	2.43	2.25	0.00	—	1.00	α_1	Y
	20	NbSi ₂ P ₄	3.53	2.27	2.52	2.23	—	—	—	α_1	Y
	21	TaSi ₂ P ₄	3.54	2.27	2.52	2.24	—	—	—	α_1	Y
	22	VGe ₂ P ₄	3.56	2.33	2.44	2.36	—	—	1.00	α_2	Y
	23	NbGe ₂ P ₄	3.62	2.35	2.53	2.36	—	—	—	α_2	Y
	24	TaGe ₂ P ₄	3.61	2.34	2.53	2.36	—	—	—	α_2	Y
34 VEC	25	CrSi ₂ N ₄	2.84	1.73	2.00	1.75	0.49(Γ -K)	0.94(K-K)	—	α_1	Y
	26	MoSi ₂ N ₄	2.91	1.75	2.09	1.75	1.74(Γ -K)	2.31(Γ -K)	—	α_1	Y
	27	WSi ₂ N ₄	2.91	1.76	2.10	1.75	2.08(Γ -K)	2.66(Γ -K)	—	α_1	Y
	28	CrGe ₂ N ₄	3.06	1.88	2.04	1.89	—	—	2.00	β_2	N
	29	MoGe ₂ N ₄	3.02	1.85	2.12	1.87	0.99(Γ K-K)	1.38(Γ K-K)	—	α_1	Y
	30	WGe ₂ N ₄	3.02	1.85	2.13	1.88	1.29(Γ K-K)	1.69(Γ K-K)	—	α_1	Y
	31	CrSi ₂ P ₄	3.41	2.23	2.37	2.27	0.34(Γ K-K)	0.65(K-K)	—	α_2	Y
	32	MoSi ₂ P ₄	3.46	2.25	2.46	2.26	0.91(K-K)	1.19(K-K)	—	α_2	Y
	33	WSi ₂ P ₄	3.46	2.25	2.46	2.26	0.86(K-K)	1.11(K-K)	—	α_2	Y
	34	CrGe ₂ P ₄	3.49	2.31	2.39	2.36	0.04(Γ K-K)	0.36(Γ K-K)	—	α_2	Y
	35	MoGe ₂ P ₄	3.53	2.32	2.47	2.34	0.56(Γ K-K)	0.95(Γ K-K)	—	α_2	Y
	36	WGe ₂ P ₄	3.54	2.32	2.47	2.35	0.63(Γ K-K)	0.89(K-K)	—	α_2	Y

Table S3, The enthalpies of formation E_f (eV/atom) of α_{1-6} - and β_{1-6} - MA_2Z_4 monolayers with space group $P\bar{6}m2$ and $P\bar{3}m1$, respectively, where $M = \text{Mg, Ca, Sr, Zn, Cd, Hg}$; $A = \text{Al and Ga}$; $Z = \text{S, Se and Te}$. It should be noticed that because the difference in E_f between β_1 - and β_2 -phase is very small, we chose four significant digits to distinguish them.

No.	Name	α_1	α_2	α_3	α_4	α_5	α_6	β_1	β_2	β_3	β_4	β_5	β_6
01	MgAl ₂ S ₄	-1.102	-1.101	-1.101	-0.856	-1.094	-0.853	-1.1525	-1.1542	-0.782	-1.037	-1.042	-0.784
02	CaAl ₂ S ₄	-1.278	-1.275	-1.250	-0.998	-1.240	-0.989	-1.2891	-1.2931	-0.512	-1.219	-1.227	-0.530
03	SrAl ₂ S ₄	-1.229	-1.226	-1.183	-0.923	-1.176	-0.914	-1.2290	-1.2329	-0.448	-1.170	-1.176	-0.919
04	ZnAl ₂ S ₄	-0.820	-0.821	-0.827	-0.591	-0.831	-0.604	-0.8854	-0.8843	-0.519	-0.768	-0.763	-0.506
05	CdAl ₂ S ₄	-0.810	-0.812	-0.792	-0.559	-0.805	-0.573	-0.8398	-0.8375	-0.523	-0.774	-0.763	-0.511
06	HgAl ₂ S ₄	-0.623	-0.628	-0.614	-0.417	-0.635	-0.431	-0.6474	-0.6429	-0.397	-0.615	-0.593	-0.387
07	MgGa ₂ S ₄	-0.804	-0.803	-0.719	-0.513	-0.715	-0.514	-0.8487	-0.8504	-0.439	-0.656	-0.657	-0.438
08	CaGa ₂ S ₄	-0.974	-0.972	-0.881	-0.431	-0.867	-0.653	-0.9827	-0.9852	-0.494	-0.845	-0.855	-0.491
09	SrGa ₂ S ₄	-0.925	-0.923	-0.823	-0.447	-0.812	-0.588	-0.9248	-0.9273	-0.475	-0.804	-0.814	-0.439
10	ZnGa ₂ S ₄	-0.526	-0.526	-0.449	-0.256	-0.459	-0.278	-0.5863	-0.5869	-0.195	-0.393	-0.379	-0.174
11	CdGa ₂ S ₄	-0.513	-0.514	-0.421	-0.224	-0.439	-0.247	-0.5400	-0.5398	-0.194	-0.405	-0.387	0.032
12	HgGa ₂ S ₄	-0.330	-0.331	-0.249	0.042	-0.276	-0.106	-0.3521	-0.3510	-0.064	-0.251	-0.221	0.207
13	MgAl ₂ Se ₄	-0.907	-0.906	-0.899	-0.674	-0.888	-0.673	-0.9531	-0.9546	-0.602	-0.835	-0.841	-0.602
14	CaAl ₂ Se ₄	-1.103	-1.100	-1.083	-0.852	-1.065	-0.838	-1.1113	-1.1152	-0.493	-1.042	-1.057	-0.520
15	SrAl ₂ Se ₄	-1.073	-1.069	-1.044	-0.807	-1.028	-0.793	-1.0720	-1.0762	-0.463	-1.018	-1.032	-0.458
16	ZnAl ₂ Se ₄	-0.653	-0.654	-0.655	-0.445	-0.655	-0.460	-0.7164	-0.7157	-0.386	-0.595	-0.588	-0.373
17	CdAl ₂ Se ₄	-0.664	-0.665	-0.649	-0.441	-0.657	-0.457	-0.6942	-0.6929	-0.407	-0.624	-0.613	-0.393
18	HgAl ₂ Se ₄	-0.507	-0.510	-0.506	0.127	-0.523	-0.353	-0.5332	-0.5302	-0.325	-0.499	-0.476	-0.324
19	MgGa ₂ Se ₄	-0.702	-0.701	-0.610	-0.418	-0.602	-0.423	-0.7428	-0.7445	-0.358	-0.549	-0.550	-0.354
20	CaGa ₂ Se ₄	-0.889	-0.887	-0.799	-0.444	-0.779	-0.583	-0.8943	-0.8971	-0.407	-0.756	-0.771	-0.507
21	SrGa ₂ Se ₄	-0.857	-0.854	-0.767	-0.460	-0.747	-0.543	-0.8554	-0.8584	-0.462	-0.737	-0.464	-0.452
22	ZnGa ₂ Se ₄	-0.452	-0.452	-0.373	-0.206	-0.380	-0.231	-0.5131	-0.5138	-0.167	-0.321	-0.302	-0.156
23	CdGa ₂ Se ₄	-0.460	-0.459	-0.369	-0.075	-0.383	-0.222	-0.4882	-0.4886	-0.173	-0.348	-0.329	-0.160
24	HgGa ₂ Se ₄	-0.307	-0.307	-0.237	0.011	-0.260	-0.118	-0.3330	-0.3331	-0.077	-0.233	-0.203	0.104
25	MgAl ₂ Te ₄	-0.480	-0.480	-0.454	-0.246	-0.442	-0.254	-0.5252	-0.5264	-0.203	-0.394	-0.394	-0.202
26	CaAl ₂ Te ₄	-0.695	-0.692	-0.667	-0.443	-0.640	-0.428	-0.7012	-0.7047	-0.239	-0.618	-0.638	-0.284
27	SrAl ₂ Te ₄	-0.688	-0.685	-0.661	-0.156	-0.634	-0.415	-0.6866	-0.6907	-0.231	-0.623	-0.644	-0.255
28	ZnAl ₂ Te ₄	-0.263	-0.264	-0.263	-0.097	-0.269	-0.113	-0.3315	-0.3307	-0.066	-0.214	-0.199	-0.071
29	CdAl ₂ Te ₄	-0.300	-0.301	-0.279	-0.108	-0.289	-0.120	-0.3366	-0.3357	-0.088	-0.254	-0.235	-0.094
30	HgAl ₂ Te ₄	-0.185	-0.187	-0.202	0.269	-0.214	-0.069	-0.2184	-0.2162	-0.057	-0.189	-0.184	-0.065
31	MgGa ₂ Te ₄	-0.372	-0.371	-0.267	-0.075	-0.267	-0.130	-0.4134	-0.4148	-0.114	-0.226	-0.219	-0.107
32	CaGa ₂ Te ₄	-0.577	-0.575	-0.473	-0.299	-0.450	-0.281	-0.5801	-0.5829	-0.292	-0.276	-0.444	-0.265
33	SrGa ₂ Te ₄	-0.567	-0.564	-0.471	-0.319	-0.444	-0.314	-0.5641	-0.5674	-0.296	-0.281	-0.453	-0.308
34	ZnGa ₂ Te ₄	-0.161	-0.161	-0.099	0.116	-0.111	-0.001	-0.2267	-0.2269	0.016	-0.059	-0.056	0.031
35	CdGa ₂ Te ₄	-0.193	-0.192	-0.110	0.058	-0.126	-0.003	-0.2279	-0.2284	0.022	-0.092	-0.081	0.026
36	HgGa ₂ Te ₄	-0.083	-0.082	0.170	0.131	-0.056	0.056	-0.1144	-0.1143	0.080	-0.025	-0.024	0.073

Table S4, Carrier mobility of α_2 -WSi₂P₄, 2H-MoS₂ and 2H-WSe₂. Deformation potential E_1 (eV), in-plane stiffness C^{2D} (N/m), effective mass m^* (m_e), mobility μ (cm² V⁻¹ s⁻¹) for electron (e) and hole (h) along a_{o1} (or zigzag) and a_{o2} (or armchair) directions (See [Figure S4](#)) at 300 K.

Compounds	carrier type	E_1	C^{2D}	m^*	μ
α_2 -WSi ₂ P ₄ (this work)	e(a_{o1})(K)	-10.90	227.49	0.43	147.22
	h(a_{o1})(K)	-6.75	227.49	0.35	466.70
	e(a_{o2})(K)	-10.71	227.74	0.43	152.66
	h(a_{o2})(K)	-6.82	227.74	0.35	457.67
MoS ₂ (this work)	e(a_{o1})(K)	-11.24	132.04	0.46	70.22
	h(a_{o1})(K)	-5.68	132.04	0.59	169.45
	e(a_{o2})(K)	-11.25	132.74	0.46	70.37
	h(a_{o2})(K)	-5.70	132.74	0.59	168.91
WSe ₂ (this work)	e(a_{o1})(K)	-10.95	119.52	0.34	119.76
	h(a_{o1})(K)	-4.92	119.52	0.47	321.87
	e(a_{o2})(K)	-10.29	119.77	0.35	130.53
	h(a_{o2})(K)	-5.03	119.77	0.47	309.92
MoS ₂ (Ref 72)	e(a_{o1})(K)	-10.88	127.44	0.46	72.16
	h(a_{o1})(K)	-5.29	127.44	0.57	200.52
	e(a_{o2})(K)	-11.36	128.16	0.48	60.32
	h(a_{o2})(K)	-5.77	128.16	0.60	152.18
WSe ₂ (Ref 34)	e(a_{o1})(K)	-10.23	121.10	0.35	135.08
	h(a_{o1})(K)	-4.65	121.10	0.46	373.65
	e(a_{o2})(K)	-10.71	120.80	0.33	—
	h(a_{o2})(K)	-4.52	120.80	0.44	—